

Document downloaded from:

<http://hdl.handle.net/10251/115303>

This paper must be cited as:

Barba, A.; Clausell, C.; Nuño Fernández, L.; Jarque, JC. (2017). ZnO and CuO crystal precipitation in sintering Cu-doped Ni-Zn ferrites. II. Influence of sintering temperature and sintering time. *Journal of the European Ceramic Society*. 37(1):169-177.
doi:10.1016/j.jeurceramsoc.2016.07.033



The final publication is available at

<http://doi.org/10.1016/j.jeurceramsoc.2016.07.033>

Copyright Elsevier

Additional Information

ZnO and CuO crystal precipitation in sintering Cu-doped Ni-Zn ferrites. II. Influence of sintering temperature and sintering time

Antonio Barba¹, Carolina Clausell^{*1}, Luis Nuño², Juan Carlos Jarque¹

¹Instituto Universitario de Tecnología Cerámica, Departamento de Ingeniería Química,
Universitat Jaume I, 12071 Castellón, Spain

²Escuela Técnica Superior de Ingenieros de Telecomunicación, Departamento de Comunicaciones
Universidad Politécnica de Valencia, 46022 Valencia, Spain

This paper presents a study of the precipitation of ZnO and CuO crystals during the sintering of Cu-doped Ni-Zn ferrites. The nature of the resulting crystal precipitates were analysed using scanning electron microscopy (SEM), energy-dispersive X-ray (EDX) analysis, X-ray diffraction (XRD), and X-ray photoelectron spectroscopy (XPS), confirming the findings of a previous paper (Part I). This study examines the influence of sintering temperature and sintering time of the thermal cycle on their formation, and on their microstructure and electromagnetic properties. The same two consecutive chemical reactions proposed in Part I can be used to explain the bulk precipitation and subsequent re-dissolution of the zinc and copper oxides observed during sintering. The effect of these crystal precipitates on the final properties of this type of soft ferrite was also analysed, revealing a deterioration in its electromagnetic performance.

Key words: ferrites, sintering, precipitation, zinc oxide, copper oxide.

I. Introduction

Ferrite powders containing nickel, zinc and different amounts of copper are typically used as electromagnetic wave absorbers. There has been a growing interest in NiCuZn ferrites, mainly because these oxides can be sintered at relatively low temperatures with a wide range of compositions. In particular, the addition of Cu in the ferrite composition has been known to play a crucial role in reducing the firing temperature and, compared to other types of ferrite, NiCuZn ferrites have better properties at high frequencies than MnZn ferrites [1–4] (such as high permeability in the RF (radio frequency) range, high electrical resistivity and environmental stability) and lower densification temperatures than NiZn ferrites [5,6].

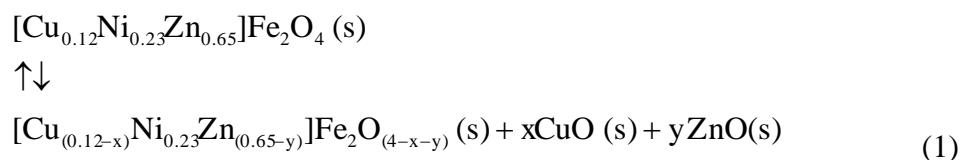
Previous papers by the present authors have addressed the synthesis, sintering [7], and final properties of Cu-doped Ni-Zn ferrites [8], establishing a thermal cycle based on sintering kinetics [9]. However, the magnetic properties of these materials are not only

determined by their chemical composition, but also by their microstructure [10–14], i.e. grain- and pore-size distribution, total porosity (or relative density), and grain-boundary characteristics. That is, the method by which the ferrites are prepared and the sintering conditions applied exert a strong influence [15].

Grain-boundary characteristics are affected by the occurrence of crystal precipitates like the ones detected in Part I of this study, where the influence of the green relative density of the Cu-doped Ni–Zn ferrites and the cooling rate of the thermal cycle on the occurring precipitates was studied [16].

In this previous paper, the authors studied crystal precipitation during sintering of a $(\text{Cu}_{0.12}\text{Ni}_{0.23}\text{Zn}_{0.65})\text{Fe}_2\text{O}_4$ ferrite, concluding that:

1. During the heating stage, depending on green relative density and the cooling rate of the thermal cycle, both rounded crystals and smaller elongated crystals can precipitate. The rounded crystals initially precipitated at triple points, then on grain boundaries and, subsequently, when the grain boundaries were saturated, inside the grains. The smaller elongated crystals precipitated around the rounded crystals.
2. The nature of the crystal precipitates was analysed using energy-dispersive X-ray (EDX), X-ray diffraction (XRD), and X-ray photoelectron spectroscopy (XPS) analysis techniques: the rounded crystal precipitates corresponded to zinc oxide, while the smaller elongated crystals corresponded to copper oxides (CuO and Cu_2O).
3. Two consecutive chemical reactions (equations 1 and 2) were proposed to explain the bulk precipitation of the zinc and copper oxides in the specimen during sintering and their subsequent re-dissolution during cooling. In equation 2, oxygen gas plays a key role, to the point where the extent to which this reaction develops (in both directions) largely depends on gas diffusion throughout the porous solid.



This paper builds on this previous study, establishing a relationship between the formation of crystal precipitates and two other sintering variables, sintering temperature and sintering time. As in the previous study, a means of avoiding the formation of crystal precipitates during sintering, or facilitating their dissolution during the cooling stage, is proposed. The effect these precipitates have on the final properties of this type of soft ferrite were also analysed, determining the imaginary part - μ'' of the complex magnetic permeability (within the operative frequency range of the material), one of the parameters used in the quality control of electromagnetic properties during production of this material [17].

II. Experimental Procedure

(1) Material preparation

The work described in this paper was conducted with the same ferrite used in the previous paper [16]. The chemical composition of the ferrite was $(\text{Cu}_{0.12}\text{Ni}_{0.23}\text{Zn}_{0.65})\text{Fe}_2\text{O}_4$. The ferrite powder, supplied by Fair-Rite Products Corp., consisted of granules with an average size of 175 μm , made up of particles with an average size of 2.1 μm , and narrow particle-size distribution (around 4 μm), and with a true density of 5380 kg/m^3 (experimentally determined on a helium pycnometer). This material was used to form cylindrical and toroidal specimens, 3 mm thick and 19 mm in external diameter (6 mm in internal diameter for the toroidal test specimens), by uniaxial dry pressing at a compaction pressure of 300 MPa.

The specimens were air sintered in an electric laboratory kiln using the same thermal cycle described in Part I [16], but varying the peak sintering temperature (hereafter, sintering temperature) between 1000 and 1200°C and remaining at this temperature for a given period of time (hereafter, sintering time) between 0 and 30 h.

The values used for compaction pressure (300 MPa) and the cooling rate (20°C/min) of the thermal cycle were selected based on the results obtained in Part I [16] in order to ensure sufficient crystal precipitation as to allow adequate observation of the effect of the two sintering variables (temperature and time) being tested in this study.

(2) Characterisation

The bulk density of the green and sintered samples was determined using the Archimedes method. The relative density (ϕ) of each ferrite specimen was calculated as the quotient

of bulk density to true density (5380 kg/m³). The average grain size (G) and distribution width (S) of the grain size distribution was determined using image analysis of the cross-sectional area of the rectangular thermally-etched surface of each cylindrical sintered specimen, observed using scanning electron microscopy (SEM). Specimens were thermally-etched in air at a temperature 100-120°C lower than their sintering temperature, for 1 hour and at a rate of 15°C/min. The width of the grain size distribution was defined as G₉₀-G₁₀, where G₉₀ and G₁₀ are those diameters below which 90 and 10 vol% of total particles lie, respectively, based on the accumulated grain size distribution curve.

The real - μ' and imaginary part - μ'' of the complex magnetic permeability was determined on an Agilent E4991A RF impedance/material analyser in the 10⁷-10⁹ Hz frequency range, using an Agilent 16454A magnetic material test fixture. In order to analyse the evolution of the electromagnetic properties against temperature and sintering time, the value of the imaginary part - μ'' at a frequency of 10⁷ Hz was selected. This value corresponds to the maximum μ'' value in the measured range (very sensitive to the microstructural changes in the samples), which is one of the parameters used in the quality control of electromagnetic properties during the production of this type of soft ferrite [17].

When analysing the crystal precipitates, the same techniques as used in Part I were applied to the sintered samples [16]. Their microstructure was observed using a scanning electron microscope - SEM (FEG-ESEM Quanta 200F) and their chemical composition was analysed via energy-dispersive X-ray (EDX) microanalysis using an analyser equipped with the SEM system. The structure of the crystals was determined by X-ray diffraction (XRD) using a PHILIPS PW1830. And finally, the binding energy of the chemical bond for each chemical element, which depends on its coordination number (crystal field) and oxidation state, was determined by X-ray photoelectron spectroscopy (XPS) using non-monochromatic 20mA and 13 kV AlK α radiation (1486.6 eV) (Sage 150 by Specs). The constant pass energy was set at 75 eV for overall analysis and 30 eV for the analysis of specific element, with a measurement area of 1x1 mm² and an chamber pressure of 7·10⁻⁹ hPa. All samples were sputtered for 5 minutes with 5 keV Argon ions prior to data collection in order to remove the adventitious carbon.

III. Results and Discussion

(1) *Microstructural and electromagnetic characterization*

The average green relative density of the compacted specimens was 0.624(1). The sintered relative density (ϕ), average grain size (G) and width of the grain size distribution (S), and the imaginary part of the complex magnetic permeability (μ'') of the specimens are shown in Table 1, within their experimental error. To enable a better understanding of the results, the evolution of the imaginary part of the relative magnetic permeability (μ'') against fired relative density (ϕ) and average grain size (G), for a sintering temperature range of 1000-1200°C and a sintering time range of 0.0-30.0 h, has been plotted in a 3D graph (Fig. 1.). From this figure, the following statements can be made:

1. An increase in both microstructural parameters, ϕ and G, leads to a higher μ'' value (as established by other authors [18]), defining a single line that asymptotically tends to a μ'' value close to 500.
2. An interrelation between the two microstructural parameters (ϕ and G) can be established. Two simultaneous processes take place during the sintering process: densification and grain growth, such that it is physically impossible to increase the relative density of a specimen without promoting the grain growth of its particles [8]. It is therefore impossible to isolate and analyse these parameters independently.
3. There is a limit G value around 20-25 μm from which the electromagnetic parameter studied significantly worsens. These experimental data correspond to those samples in which heterogeneous and exaggerated grain growth was observed (sintering temperatures of 1150 and 1200°C), as evidenced by the large values of average grain size and width of the grain size distributions. As reported in the literature [18], the exaggerated grain growth accelerates as temperature increases, hindering the migration of the pore to the grain boundary, and thereby contributing to the reduction of sintered density observed at higher temperatures. There are two main reasons why the magnetic properties worsen beyond this G limit value. Firstly, larger grains usually have pores within grains, which increases the number of pinning sites and hinders the domain wall motion, thereby reducing magnetic permeability [19]. This is the case with the specimens sintered at 1150 and 1200°C, as can be observed in Table 1 and in the SEM micrographs in Fig. 2. Specifically, these latter show a lower sintered relative density (compared with precedent sintering temperatures) and a high density of pores within grains,

although, as can be observed in Fig. 3., they are partially hidden by the crystal precipitates. Secondly, grain boundaries in polycrystalline ferrites normally act as a sink of impurities, structural disorders and defects, and a centre for precipitated non-magnetic phases, which impede the rotation of spins and the motion of the domain walls, resulting in a sample with a lower effective initial permeability [20]. These non-magnetic second phases, found mainly in the samples sintered at 1150 and 1200°C (see Fig. 3), are undoubtedly one of the factors behind the deterioration in electromagnetic properties of ferrites sintered at these two maximum temperatures.

(2) *SEM results*

Figs. 2 and 3 (SEM micrographs) show the cross-sectional microstructure evolution of the specimens (inner region) against sintering time and sintering temperature, respectively. Fig. 4 schematically illustrates the area occupied by the precipitated crystals at the sintering temperatures and times tested. The white areas correspond to regions free of crystal precipitates, while the dotted areas correspond to regions occupied by crystal precipitates. The greater the dot density, the greater the density of crystal precipitates observed in the sample. The micrographs point to the following conclusions:

1. Certain ferrite sintering conditions lead to the formation of crystal precipitates, though no crystal precipitates were detected at the lowest sintering temperature tested (1000°C). For higher sintering temperatures, crystal density and affected area increased with sintering time up to a maximum value. When sintering time was further prolonged, both crystal density and the affected area decreased and, sometimes, even completely disappeared. Meanwhile, for a given sintering time, crystal density and affected area increased with sintering temperature.
2. During crystal precipitation, crystals occur first at triple joint points, then on grain boundaries and, finally, when the triple joint points and grain boundaries are saturated, inside the ferrite grains, as was also observed in Part I [16].
3. The highest density of crystal precipitates was observed in the inner area (as in the previous paper [16], where the effect of cooling rate was studied), while the lowest density was found in the outer area, suggesting that the crystals had either precipitated from the inner to the outer area, or were moved after precipitation from the outer to the inner area.

4. Round as well as needle-shaped crystal precipitates were observed (as previously reported [16]), with round crystal precipitates being the first to form at low densities. As crystal density increased (either by raising sintering temperature or prolonging sintering time, though always below the maximum sintering time), the needle-shaped crystal precipitates begin to appear. The first needle-shaped precipitates formed around the round precipitates and, when the surfaces of these latter are saturated, they begin to appear inside the ferrite grains.

The formation and cross-sectional distribution of the crystal precipitates can be understood if the following explanation is accepted.

In the earlier study [16] it was observed that crystal precipitation increased along with the relative density of the unfired samples and the cooling rate of the thermal cycle. In the present study it has been observed that the concentration of crystal precipitates also increases with sintering temperature and sintering time. In this case, however, it emerges that, for a sufficiently long sintering time, the density of the crystal precipitates actually begins to decrease, or even completely disappears, above a given sintering temperature.

Part I [16] showed that crystal precipitation occurred during the densification and grain-growth stages when these stages were developed with an oxygen deficiency (as would be the case of specimens with high relative density, in which pore size distribution is thin and narrow, and the network that is formed between particles is more tortuous, making gas access difficult). Additionally, when the cooling stage was prolonged enough to allow oxygen to enter the sample (as in the case of the lowest cooling rate tested), the re-dissolution of the crystal precipitates during the cooling stage was also taken into consideration.

In the present study it has been observed that the presence of crystal precipitates in the specimens in terms of crystal density and affected area increases with sintering temperature, which matches that observed in the $\text{Fe}_2\text{O}_3\text{-ZnO-NiO}$ ternary phase diagram mentioned in Part I [16], and passes through a maximum with sintering time. The $\text{Fe}_2\text{O}_3\text{-ZnO-NiO}$ ternary phase diagram shows a $\text{ZnO} + (\text{Zn,Ni})\text{Fe}_2\text{O}_4$ ss + $(\text{Ni,Zn})\text{O}$ ss area, that is very close to our composition (without the Cu content), in the temperature range of 950-1180°C. Although the corresponding quaternary phase diagram could not be found in the literature, the behaviour of this phase might be expected to resemble that of Ni-Zn ferrites, and the ferrite composition might be expected to play the same determining role in the possible precipitation of ZnO and certain other crystalline phases during sintering.

When the evolution of the relative density of the sintered samples as a function of sintering time, shown in Table 1, is compared with the precipitation scheme depicted in Fig. 4, it can be observed that, for each temperature tested, the time at which crystal precipitates begin to be detected corresponds to relative densities of around 0.95. This suggests that the influence of sintering time on the density of the crystal precipitates and affected area also stem from the oxygen concentration in the sample. At sintering onset, the porosity of the sample (defined as $1-\phi$) is greater and its pore structure less tortuous and more accessible from the outside, which allows a continuous inflow of oxygen into the sample. As the sintering stage progresses, the porosity of the specimen decreases, the sample shrinks, and the tortuosity of the pore structure increases, leaving isolated pores inside it. This new structure makes it more difficult for the oxygen to access the inner region of the sample, causing crystal precipitation to begin in this area. However, when sintering time is long enough, oxygen is able to penetrate into the sample (gas diffusion), triggering the dissolution of the previously precipitated crystals, thereby decreasing the overall density of crystal precipitates in the sample and even, at sufficiently long sintering times, causing the precipitates to completely re-dissolve (as occurred at a temperature of 1100°C). Needle-shaped crystals were observed to dissolve before the round ones.

(3) *EDX, XRD, and XPS results*

In order to identify the composition of the crystal precipitates detected by SEM, three experimental techniques were used: energy-dispersive X-ray (EDX) microanalysis, X-ray diffraction (XRD) analysis, and X-ray photoelectron spectroscopy (XPS).

Fig. 5 shows the microstructure and grain boundaries of a sintered specimen with crystal precipitates. Three different regions may be distinguished, which have been labelled as follows:

F: (grey) ferrite matrix

Z: (light-coloured) round crystal precipitates located on the grain surface, on the grain boundaries, and at triple joint points

C: needle-shaped crystal precipitates (lighter-coloured than the Z crystal precipitates) located on the grain surface and around Z crystal precipitates.

The EDX analyses of the three different regions, as previously reported [16], suggest that:

1. The average chemical composition of specimens with and without crystal precipitates is very similar to the chemical composition of the ferrite powder. In

the case of the specimen with crystal precipitates, a small increase in the Zn peak is noted.

2. The point chemical composition of the F area is also similar to the average chemical composition of the specimen without crystal precipitates and to that of the ferrite powder.
3. The point chemical composition of the Z crystal precipitates displays a very significant increase in the Zn peak, while the point chemical composition of the C crystal precipitates similarly exhibits a considerable rise in the Cu peak. These results suggest that the Z crystal precipitates are zinc oxide crystals, and the C crystal precipitates are copper oxide crystals.

As previously reported [16], and as shown in Fig. 6, an XRD analysis of the cross-sectional area of the rectangular etched surface containing crystal precipitates (sample referred to as WITH) allowed identification of two crystal structures: franklinite (corresponding to the ferrite) and zincite (corresponding to zinc oxide). The zincite structure matches the EDX results of the Z crystal precipitates, which formed primarily in the inner area. No crystal structure corresponding to the C crystal precipitates was identified. However, this can likely be ascribed to the fact that C crystal concentration is much lower than Z crystal concentration.

Fig. 7 shows the peaks (including the Auger peaks) in XPS spectra of the cross-section of two sintered specimens, with and without crystal precipitates. It can be observed that zinc and copper contents are higher in the sample containing crystal precipitates than in that the sample without. The XPS semi-quantitative analysis shows a 4.1 mol% Cu and 17.2 mol% Zn in the sample with crystal precipitates versus a 1.3 mol% Cu and 10.8 mol% Zn in the sample without.

The enclosed area inside each of the high intensity peaks (Zn 2p, Zn LMM, Cu 2p, Ni 2p, Fe 2p, and O 1s) was quantified, taking into account the sensitivity factors proposed by the CasaXPS software for data treatment [21,22], and the results of the deconvolution of the Zn 2p, Cu 2p and O 1s peaks are shown in Table 2.

These XPS results, as with those previously reported [16], suggest:

1. Ni and Fe are only present in the ferrite structure and not in the crystal precipitates for both of the samples tested.

2. Cu appears in the ferrite structure in both spectra. However, the spectrum of the specimen with crystal precipitates also exhibits peaks corresponding to the Cu-O chemical bond in CuO and, likely also, in Cu₂O.

The contribution of the Zn-O bond in the ferrite appears in both specimens. For the specimen with crystal precipitates, the contribution of the Zn-O bond in the ZnO compound needs to be considered.

3. Two contributions should be considered in the specimens without crystal precipitates to explain the two different (octahedral and tetrahedral) sites defined by the oxygen network. In the specimens with crystal precipitates, an additional contribution needs to be considered, which again confirms the joint occurrence of copper and zinc oxides in the ferrite structure.

Based on the deconvoluted XPS peaks studied and the XPS semi-quantitative analysis results, atomic composition of the crystal precipitates can be estimated at 12.7 mol% oxygen, 10.5 mol% zinc and 2.2 mol% copper in two different chemical compounds: CuO and Cu₂O. Therefore, the crystal precipitates found in the ferrite likely contain ZnO, CuO, and Cu₂O. Zinc oxide may be estimated at around 24 wt%, cupric oxide at about 3wt% and cuprous oxide at about 2wt%.

(4) Comments

Under certain conditions, crystal precipitates can occur when Cu-doped Ni-Zn [16,23–25] or Mn-Zn ferrites are sintered. However, contrary to that suggested in the literature [26], zinc loss (and its subsequent precipitation) can be observed in samples prepared using a different process besides the hydrothermal route, as was observed in this study.

Cooling speed seems to have a marked influence on the occurrence of crystal precipitates, affecting the kinetics of the precipitation process, while oxygen concentration was also found to have a determining influence. Higher green relative density causes lower open porosity, leading to closed porosity in the first sintering stage. This resulting closed porosity blocks oxygen from entering the structure. Similarly, slow cooling rates allow oxygen into the pores better than fast cooling. Green relative density and cooling rate are, therefore, both determining factors in the presence or absence of oxygen inside the pores.

In the present study it was observed that higher sintering temperatures led to a higher occurrence and/or density of crystal precipitates, which impacted on the system's thermodynamics. The same statement can be made for the influence of sintering time,

though in this case only up to a maximum time, beyond which the density of the crystal precipitates and/or the affected area decreased.

Sintering temperature and sintering time (as well as green relative density and cooling speed) have a marked influence on the occurrence of crystal precipitates. As in the previous paper [16], the results in the present study are consistent with ZnO and CuO precipitation (with the possible subsequent reduction of Cu(II) to Cu(I)) being largely dependent on the oxygen concentration in the pores. The chemical reactions proposed (reactions 1 and 2) are again consistent with the experimental data obtained in this study, as well as with those reported in the literature [23–25]. As was stated in the previous part, a Fe₂O₃-ZnO-NiO-CuO quaternary phase diagram would probably explain the marked dependence of reaction (1) on composition and temperature, just as the Fe₂O₃-ZnO-NiO ternary phase diagram explains this dependence in the case of Ni-Zn ferrites. Also as mentioned in Part I^[16], the CuO obtained in reaction (1) is unstable at high temperatures, as reported in the traditional chemistry literature [27,28]. Therefore, the decomposition shown in reaction (2) should be developed.

Consequently, the formation of zinc and copper oxide crystal precipitates could be due to the sintering process being faster than the rate of oxygen diffusion from outside into the pores. The absence of oxygen inside the pores leads to the proposed chemical reactions, resulting in the bulk precipitation of ZnO and CuO and the transformation of CuO to Cu₂O. After the densification and grain-growth stage, and in the cooling stage, the proposed chemical reactions might shift to the left, depending on how much oxygen enters the pores. This process becomes more important when specimen porosity is high enough, the thermal cycle is long enough and/or the cooling speed low enough to allow oxygen diffusion in all cases, even where the diffusion coefficient is small. The net effect is the re-dissolution of crystal precipitates in the ferrite crystal structure, proceeding from the outermost area inwards.

As seen in Fig. 1, the imaginary part of the complex magnetic permeability (μ'') worsens with the occurrence of crystal precipitates. Some authors suggest [23,24,29] that when zinc oxide loss occurs, grain boundary migration might be increased, resulting in the formation of giant grains. In the present study, it has been observed that the higher the grain growth, the higher the density of crystal precipitates, suggesting that, as indicated in the literature, a relationship must exist between the zinc loss and the grain growth of the microstructure.

As grain size increases, multi-domain grains are obtained, which leads to higher permeability values due to the domain wall contribution [30,31], provided that there is no evidence for exaggerated or abnormal grain growth. Also, an increase in the sintered relative density of the ceramics not only results in the reduction of the demagnetizing field due to the elimination of pores, but also raises the spin rotational contribution, which in turn increases permeability [32].

When grain growth is high, the mobility of the grain boundaries is higher than pore mobility. This means that the pores are left behind, resulting in pores that are trapped inside (intraporosity), and not between (interporosity), the grains. This intragrain porosity, which is practically impossible to eliminate, hinders the magnetization process by pinning the domain [33], reducing the permeability of the material [19]. Moreover, crystals precipitates at the grain boundaries inhibit the rotation of spins, making domain wall motion and domain rotation difficult and leading to a decrease in the effective initial permeability of the sample [34].

IV. Conclusions

The occurrence of crystal precipitates was found to vary with sintering temperature and sintering time. Crystal density and affected area were observed to increase against sintering temperature (except for the lowest temperature of 1000°C) and with sintering time, though in the case of the latter this is true only until a maximum value is reached. Beyond this maximum, both crystal density and affected area decrease and, in some cases, the precipitates completely disappeared.

The results obtained in this and the previous study suggest that the precipitation of zinc oxide (ZnO) and copper oxide (CuO and Cu₂O) crystals during the sintering of Cu-doped Ni-Zn ferrites occurred during the densification and grain-growth stages, when these stages are developed with an oxygen deficiency. This oxygen deficiency in turn depended on the microstructure of the sample. So, when pore size distribution is finer and narrower, and the network formed between the particles is more tortuous, making it difficult for oxygen to enter, the oxygen concentration inside the sample decreases, leading to the observed crystal precipitation. However, the results obtained also indicate that the partial or total dissolution of these crystal precipitates can also occur during the cooling stage, provided that this stage is long enough to allow oxygen to enter the sample.

It has also been observed that crystal precipitates, which mainly occur at the grain boundaries, worsen the electromagnetic performance of these ferrites, hindering the magnetization process through the inhibition of spin rotation and domain wall motion.

Acknowledgements

The study has been conducted with funding from the project MAT2008-05590, within the scope of the 6th Spanish National Plan for Scientific Research, Development, and Technology Innovation 2008–2011, and the project P1·1B2012-13, within the scope of the Pla de Promoció de la Investigació de la Universitat Jaume I 2012.

References

- [1] B. Li, Z.X. Yue, X.W. Qi, J. Zhou, Z.L. Gui, L.T. Li, High Mn content NiCuZn ferrite for multiplayer chip inductor application, *Mater. Sci. Eng. B Solid-State Mater. Adv. Technol.* 99 (2003) 252–254. doi:10.1016/S0921-5107(02)00489-0.
- [2] T. Krishnaveni, B.R. Kanth, V.S.R. Raju, S.R. Murthy, Fabrication of multilayer chip inductors using Ni-Cu-Zn ferrites, *J. Alloys Compd.* 414 (2006) 282–286. doi:10.1016/j.jallcom.2005.07.029.
- [3] H. Su, H. Zhang, X. Tang, Y. Jing, Effects of calcining temperature and heating rate on properties of high-permeability NiCuZn ferrites, *J. Magn. Magn. Mater.* 302 (2006) 278–281. doi:10.1016/j.jmmm.2005.09.033.
- [4] C. Sujatha, K. Venugopal Reddy, K. Sowri Babu, A. Ramachandra Reddy, K.H. Rao, Effect of sintering temperature on electromagnetic properties of NiCuZn ferrite, *Ceram. Int.* 39 (2013) 3077–3086. doi:10.1016/j.ceramint.2012.09.087.
- [5] D. Stoppels, Developments in soft magnetic power ferrites, *J. Magn. Magn. Mater.* 160 (1996) 323–328. doi:10.1016/0304-8853(96)00216-8.
- [6] H.-M. Sung, C.-J. Chen, L.-J. Wang, W.-S. Ko, The characteristics of low temperature co-fired multilayer chip LC filters, *IEEE Trans. Magn.* 34 (1998) 1363 – 1365.
- [7] A. Barba, C. Clausell, C. Felú, M. Monzó, Sintering of (Cu_{0.25}Ni_{0.25}Zn_{0.50})Fe₂O₄Ferrite, *J. Am. Ceram. Soc.* 77 (2004) 571–577.
- [8] A. Barba, C. Clausell, C. Felú, M. Monzó, L. Nuño, D. Heras, J. V. Balbastre, L. Nuño, A. Barba, J. V. Balbastre, C. Clausell, A. Viñes, Study of NiZn ferrite complex permeability: Effect of relative density and microstructure, *J. Am. Ceram. Soc.* 87 (2004) 1314–1318. doi:10.1111/j.1151-2916.2004.tb07727.x.
- [9] A. Barba, C. Clausell, M. Monzó, J.C. Jarque, M. Monzó, J.C. Jarque, Thermal cycle for obtaining a Ni-Zn ferrite: (I) Design of the sintering stage, *Boletín La Soc. Española Cerámica Y Vidr.* 47 (2008) 13–23. doi:10.3989 / cyv.2004.v43.i5.
- [10] B. Domenichini, T. Caillot, Sintering of Fe₂NiO₄ with an internal binder: a way to obtain a very dense material, *Acta Mater.* 51 (2003) 4815–4821. doi:10.1016/S1359-6454(03)00321-5.
- [11] M. Rozman, M. Drogenik, Sintering of nanosized MnZn ferrite powders, *J. Am. Ceram. Soc.* 81 (1998) 1757–1764. doi:10.1111/j.1151-2916.1998.tb02545.x.
- [12] S. Corso, P. Tailhades, I. Pasquet, A. Rousset, V. Laurent, A. Gabriel, C. Condolf, Preparation conditions of pure and stoichiometric Ni_xFe_{3-x}O₄ bulk ceramics, *Solid State Sci.* 6 (2004) 791–798. doi:10.1016/j.solidstatesciences.2004.03.037.
- [13] A.K.M. Akther Hossain, M.L. Rahman, Enhancement of microstructure and initial permeability due to Cu substitution in Ni_{0.50-x}Cu_xZn_{0.50}Fe₂O₄ ferrites, *J. Magn. Magn. Mater.* 323 (2011) 1954–1962. doi:10.1016/j.jmmm.2011.02.031.
- [14] J. Mürbe, J. Töpfer, Low temperature sintering of sub-stoichiometric Ni–Cu–Zn ferrites: Shrinkage, microstructure and permeability, *J. Magn. Magn. Mater.* 324 (2012) 578–583. doi:10.1016/j.jmmm.2011.08.040.
- [15] M. Aliuzzaman, M. Manjurul Haque, M. Jannatul Ferdous, S. Manjura Hoque, M. Abdul Hakim, Effect of sintering time on the structural, magnetic and electrical transport properties of

- Mg_{0.35}Cu_{0.20}Zn_{0.45}Fe_{1.94}O₄ ferrites, *World J. Condens. Matter Phys.* 4 (2014) 13–23.
- [16] A. Barba, C. Clausell, J.C. Jarque, M. Monzó, ZnO and CuO crystal precipitation in sintering Cu-doped Ni-Zn ferrites. I. Influence of dry relative density and cooling rate, *J. Eur. Ceram. Soc.* 31 (2011) 2119–2128. doi:10.1016/j.jeurceramsoc.2011.05.007.
- [17] A. Verma, T.C. Goel, R.G. Mendiratta, Frequency variation of initial permeability of NiZn ferrites prepared by the citrate precursor method, *J. Magn. Magn. Mater.* 210 (2000) 274–278. doi:10.1016/S0304-8853(99)00451-5.
- [18] S.-F. Wang, Y.-R. Wang, T.C. Yang, P.-J. Wang, C.-A. Lu, Densification and properties of fluxed sintered NiCuZn ferrites, *J. Magn. Magn. Mater.* 217 (2000) 35–43. doi:10.1016/S0304-8853(00)00325-5.
- [19] J. Jeong, H.H. Han, B.C. Moon, Effects of Bi₂O₃ addition on the microstructure and electromagnetic properties of NiCuZn ferrites, *J. Mater. Sci. Mater. Electron.* 15 (2004) 303–306.
- [20] C. Clausell, A. Barba, L. Nuño, J.C. Jarque, Effect of average grain size and sintered relative density on the imaginary part – μ'' of the complex magnetic permeability of (Cu_{0.12}Ni_{0.23}Zn_{0.65})Fe₂O₄ system, *Ceram. Int.* 42 (2016) 4256–4261. doi:10.1016/j.ceramint.2015.11.101.
- [21] D. Briggs, *Handbook of X-ray Photoelectron Spectroscopy* C. D. Wanger, W. M. Riggs, L. E. Davis, J. F. Moulder and G. E. Muilenberg Perkin-Elmer Corp., Physical Electronics Division, Eden Prairie, Minnesota, USA, 1979. 190 pp. \$195, *Surf. Interface Anal.* 3 (1981) v–v. doi:10.1002/sia.740030412.
- [22] J.R. Rumble, D.M. Bickham, C.J. Powell, The NIST x-ray photoelectron spectroscopy database, *Surf. Interface Anal.* 19 (1992) 241–246. doi:10.1002/sia.740190147.
- [23] K. Majima, M. Hasegawa, S. Katsuyama, H. Nagai, S. Mishima, ZnO precipitation during sintering of Ni-Zn ferrite used for the substrate of thin-film heads, *J. Mater. Sci. Lett.* 12 (1993) 185–187.
- [24] K. Majima, M. Hasegawa, M. Yokota, S. Mishima, H. Nagai, Microstructural control of Ni-Zn ferrites for thin film heads, *Mater. Trans. JIM.* 34 (1993) 556–562.
- [25] K. Majima, M. Hasegawa, S. Katsuyama, S. Mishima, H. Nagai, Influence of composition and oxygen partial pressure in sintering atmosphere on microstructure and magnetic properties of Ni-Zn ferrite for thin film magnetic recording heads, *Mater. Trans. JIM.* 36 (1995) 1392–1397.
- [26] C. Rath, S. Anand, R.P. Das, K.K. Sahu, S.D. Kulkarni, S.K. Date, N.C. Mishra, Dependence on cation distribution of particle size, lattice parameter, and magnetic properties in nanosize Mn-Zn ferrite, *J. Appl. Phys.* 91 (2002) 2211–2215. doi:10.1063/1.1432474.
- [27] F.A. Cotton, The elements of the first transition series, in: *Adv. Inorg. Chem.*, JohnWiley&Sons Corporation, New York, 1999; pp. 801–922.
- [28] A.G. Massey, N.R. Thompson, B.F.G. Johnson, R. Davis, *Comprehensive Inorganic Chemistry*, in: *Chem. Copper, Silver Gold*, 1973. doi:10.1016/B978-0-08-018860-7.50002-5.
- [29] M. Drogenik, S. Besenicar, Reexamination of the grain size/permeability relation in high permeability Mn-Zn ferrites, *Am. Ceram. Soc. Bull.* 65 (n.d.) 656–659. <http://cat.inist.fr/?aModele=afficheN&cpsid=8741938> (accessed July 20, 2016).
- [30] T. Nakamura, Low-temperature sintering of Ni-Zn-Cu ferrite and its permeability spectra, *J. Magn. Magn. Mater.* 168 (1997) 285–291. doi:10.1016/S0304-8853(96)00709-3.
- [31] R. Lebourgeois, C. Le Fur, M. Labeyrie, M. Paté, J.P. Ganne, Permeability mechanisms in high frequency polycrystalline ferrites, *J. Magn. Magn. Mater.* 160 (1996) 329–332. doi:10.1016/0304-

8853(96)00217-X.

- [32] J.J. Shrotri, S.D. Kulkarni, C.E. Deshpande, A. Mitra, S.R. Sainkar, P.S. Anil Kumar, S.K. Date, Effect of Cu substitution on the magnetic and electrical properties of Ni–Zn ferrite synthesised by soft chemical method, *Mater. Chem. Phys.* 59 (1999) 1–5. doi:10.1016/S0254-0584(99)00019-X.
- [33] J.W. Fan, F.K. Ng, F.R. Sale, Magnetic properties and microstructures of SnO₂ doped Mn-Zn ferrites, *Rare Met.* 25 (2006) 445–449.
- [34] M.D. Rahaman, M. Dalim Mia, M.N.I. Khan, A.K.M. Akther Hossain, Study the effect of sintering temperature on structural, microstructural and electromagnetic properties of 10% Ca-doped Mn_{0.6}Zn_{0.4}Fe₂O₄, *J. Magn. Magn. Mater.* 404 (2016) 238–249. doi:10.1016/j.jmmm.2015.12.029.

Figures and tables captions

Table 1. Evolution of fired relative density (ϕ), average grain size (G), width of the grain size distribution (S) and the imaginary part of the relative magnetic permeability (μ'') with sintering temperature and sintering time.

Table 2. Deconvolution of the Zn 2p, Cu 2p and O 1s XPS diagram of a sintered specimen with crystal precipitates.

Fig. 1. Evolution of the imaginary part of the relative magnetic permeability (μ'') with fired relative density (ϕ) and average grain size (G), for a sintering temperature range of 1000-1200°C and a sintering time range of 0.0-30.0 h (see data in Table 1).

Fig. 2. Evolution of the microstructure of the samples against sintering time at a sintering temperature of 1100°C: (a) 0 h, (b) 0.2 h, (c) 0.5 h, (d) 1 h, (e) 2 h, (f) 5 h, (g) 15 h and (h) 30 h.

Fig. 3. Evolution of the microstructure of the samples against sintering temperature at a sintering time of 5 h: (a) 1000°C, (b) 1025°C, (c) 1050°C, (d) 1075°C, (e) 1100°C, (f) 1150°C and (g) 1200°C.

Fig. 4. Evolution of the cross-sectional area occupied by crystal precipitates and precipitated crystal density against sintering temperature and sintering time.

Fig. 5. Cross-sectional SEM micrograph showing the microstructure and grain boundaries of a sintered specimen with crystal precipitates.

Fig. 6. XRD diffractograms of two sintered specimens, with and without crystal precipitates.

Fig. 7. Cross-sectional XPS spectra of two sintered specimens, with and without crystal precipitates.

Table 1

Evolution of fired relative density (ϕ), average grain size (G), width of the grain size distribution (S) and the imaginary part of the relative magnetic permeability (μ'') with sintering temperature and sintering time.

T (°C)	t (h)	ϕ	G (μm)	S (μm)	μ''
1000	0	0.676 ± 0.002	1.20 ± 0.05	1.43 ± 0.05	20 ± 10
	0.2	0.710 ± 0.003	1.11 ± 0.08	1.31 ± 0.08	42 ± 10
	0.5	0.746 ± 0.003	1.23 ± 0.06	1.31 ± 0.06	75 ± 10
	1	0.782 ± 0.002	1.51 ± 0.05	1.62 ± 0.05	131 ± 10
	2	0.828 ± 0.001	1.60 ± 0.05	1.75 ± 0.05	204 ± 10
	5	0.888 ± 0.003	2.2 ± 0.1	2.5 ± 0.1	318 ± 10
	15	0.942 ± 0.001	4.1 ± 0.2	5.9 ± 0.2	429 ± 10
	30	0.955 ± 0.001	6 ± 5	11 ± 5	465 ± 10
1025	0	0.705 ± 0.004	1.36 ± 0.06	1.56 ± 0.06	31 ± 15
	0.2	0.756 ± 0.004	1.38 ± 0.06	1.54 ± 0.06	72 ± 15
	0.5	0.810 ± 0.003	1.51 ± 0.09	1.61 ± 0.09	159 ± 15
	1	0.857 ± 0.009	1.9 ± 0.1	2.1 ± 0.1	233 ± 15
	2	0.901 ± 0.005	2.8 ± 0.1	3.2 ± 0.1	325 ± 15
	5	0.941 ± 0.002	4.3 ± 0.2	7.3 ± 0.2	413 ± 15
	15	0.960 ± 0.001	11 ± 1	25 ± 1	466 ± 15
	30	0.963 ± 0.001	12 ± 5	29 ± 5	496 ± 15
1050	0	0.735 ± 0.003	1.19 ± 0.06	1.35 ± 0.06	57 ± 15
	0.2	0.812 ± 0.005	1.26 ± 0.04	1.32 ± 0.04	153 ± 15
	0.5	0.871 ± 0.003	1.94 ± 0.07	2.12 ± 0.07	284 ± 15
	1	0.914 ± 0.004	3.4 ± 0.2	4.1 ± 0.2	364 ± 15
	2	0.938 ± 0.002	4.9 ± 0.6	7.3 ± 0.6	430 ± 15
	5	0.955 ± 0.001	9.0 ± 0.8	14.0 ± 0.8	455 ± 15
	15	0.965 ± 0.001	14 ± 1	19 ± 1	497 ± 15
	30	0.963 ± 0.001	19 ± 3	22 ± 3	509 ± 15
1075	0	0.782 ± 0.004	1.11 ± 0.04	1.33 ± 0.04	119 ± 20
	0.2	0.871 ± 0.006	2.1 ± 0.3	2.5 ± 0.3	269 ± 20
	0.5	0.922 ± 0.004	5.0 ± 0.5	6.3 ± 0.5	376 ± 20
	1	0.941 ± 0.001	6.6 ± 0.3	8.4 ± 0.3	421 ± 20
	2	0.953 ± 0.001	10.0 ± 0.7	12.4 ± 0.7	443 ± 20
	5	0.961 ± 0.001	12.7 ± 0.9	15.6 ± 0.9	485 ± 20
	15	0.966 ± 0.001	16.0 ± 0.9	20.1 ± 0.9	515 ± 20
	30	0.963 ± 0.001	19.0 ± 0.6	23.9 ± 0.6	524 ± 20
1100	0	0.830 ± 0.006	1.6 ± 0.1	1.7 ± 0.1	181 ± 20
	0.2	0.914 ± 0.004	5.1 ± 0.5	6.0 ± 0.5	369 ± 20
	0.5	0.943 ± 0.001	7.6 ± 0.4	8.1 ± 0.4	422 ± 20
	1	0.953 ± 0.001	10.4 ± 0.4	10.8 ± 0.4	457 ± 20
	2	0.957 ± 0.001	14 ± 1	16 ± 1	483 ± 20
	5	0.964 ± 0.001	17.1 ± 0.6	21.0 ± 0.6	506 ± 20
	15	0.964 ± 0.001	20.3 ± 0.8	23.0 ± 0.8	526 ± 20
	30	0.967 ± 0.001	22.0 ± 0.9	26.2 ± 0.9	532 ± 20
1150	0	0.935 ± 0.002	4.7 ± 0.1	3.9 ± 0.1	382 ± 25
	0.2	0.956 ± 0.001	100 ± 10	113 ± 10	405 ± 25
	0.5	0.958 ± 0.001	131 ± 8	136 ± 8	428 ± 25
	1	0.958 ± 0.001	129 ± 10	157 ± 10	437 ± 25
	2	0.958 ± 0.001	146 ± 10	138 ± 10	445 ± 25
	5	0.958 ± 0.001	150 ± 40	173 ± 40	466 ± 25
	15	0.961 ± 0.001	126 ± 8	199 ± 8	472 ± 25
	30	0.958 ± 0.001	130 ± 8	134 ± 8	473 ± 25
1200	0	0.957 ± 0.001	110 ± 50	130 ± 50	379 ± 25
	0.2	0.959 ± 0.001	130 ± 7	158 ± 7	379 ± 25
	0.5	0.958 ± 0.001	124 ± 8	138 ± 8	393 ± 25
	1	0.958 ± 0.001	138 ± 2	165 ± 2	392 ± 25
	2	0.958 ± 0.001	115 ± 20	143 ± 20	357 ± 25
	5	0.959 ± 0.001	100 ± 10	155 ± 10	417 ± 25
	15	0.958 ± 0.001	118 ± 2	129 ± 2	472 ± 25
	30	0.953 ± 0.001	116 ± 3	135 ± 3	469 ± 25

Table 2**Deconvolution of the Zn 2p, Cu 2p and O 1s XPS diagram of a sintered specimen with crystal precipitates.**

Chemical element	Peak position (binding energy, eV)			mol%
	Zn 2p _{3/2}	Zn 2p _{1/2}	Energy difference	
Zn in ferrite	1018.9	1042.0	23.1	38.9
Zn in ZnO	1018.7	1041.5	22.8	61.1
	Cu 2p _{3/2}	Cu 2p _{1/2}	Energy difference	
Cu in ferrite	930.0	949.5	19.5	46.4
Cu in CuO	932.1	951.9	19.8	32.2
Cu in Cu ₂ O	930.5	950.1	19.8	21.4
	O 1s			
O in ferrite	529.5 and 530.8			77.4
O in precipitates	530.3			22.6

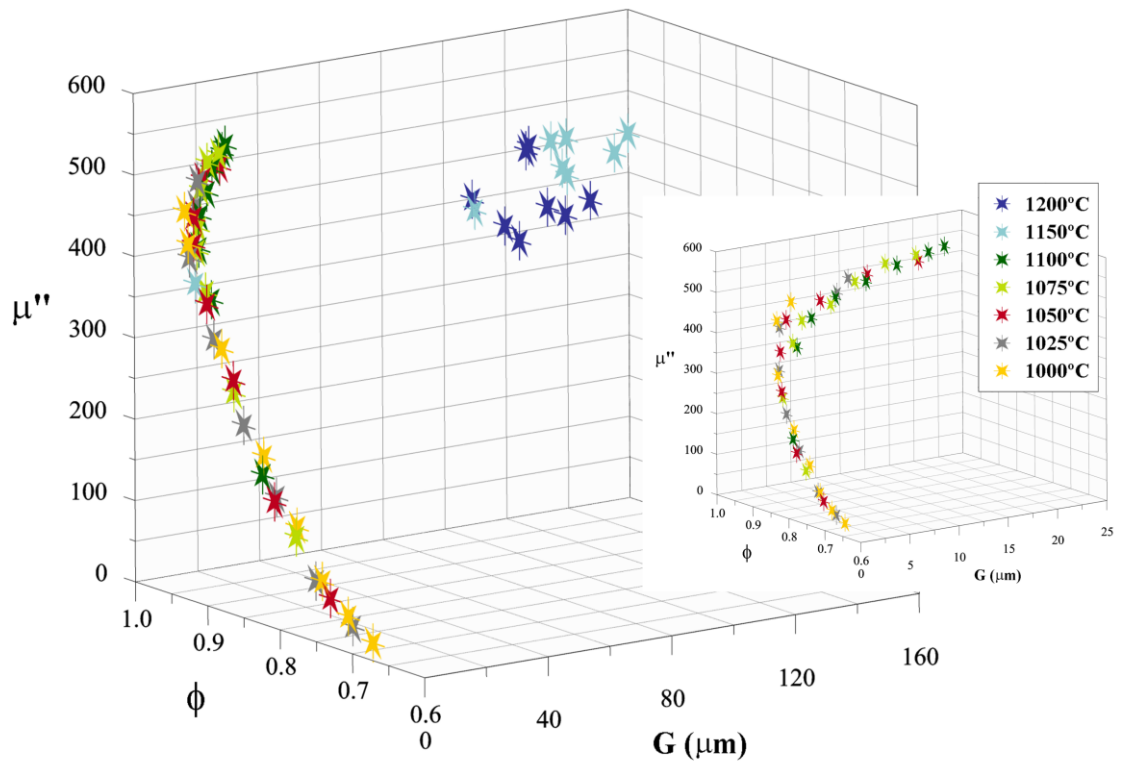


Fig. 1. Evolution of the imaginary part of the relative magnetic permeability (μ'') with fired relative density (ϕ) and average grain size (G), for a sintering temperature range of 1000-1200°C and a sintering time range of 0.0-30.0 h (see data in Table 1).

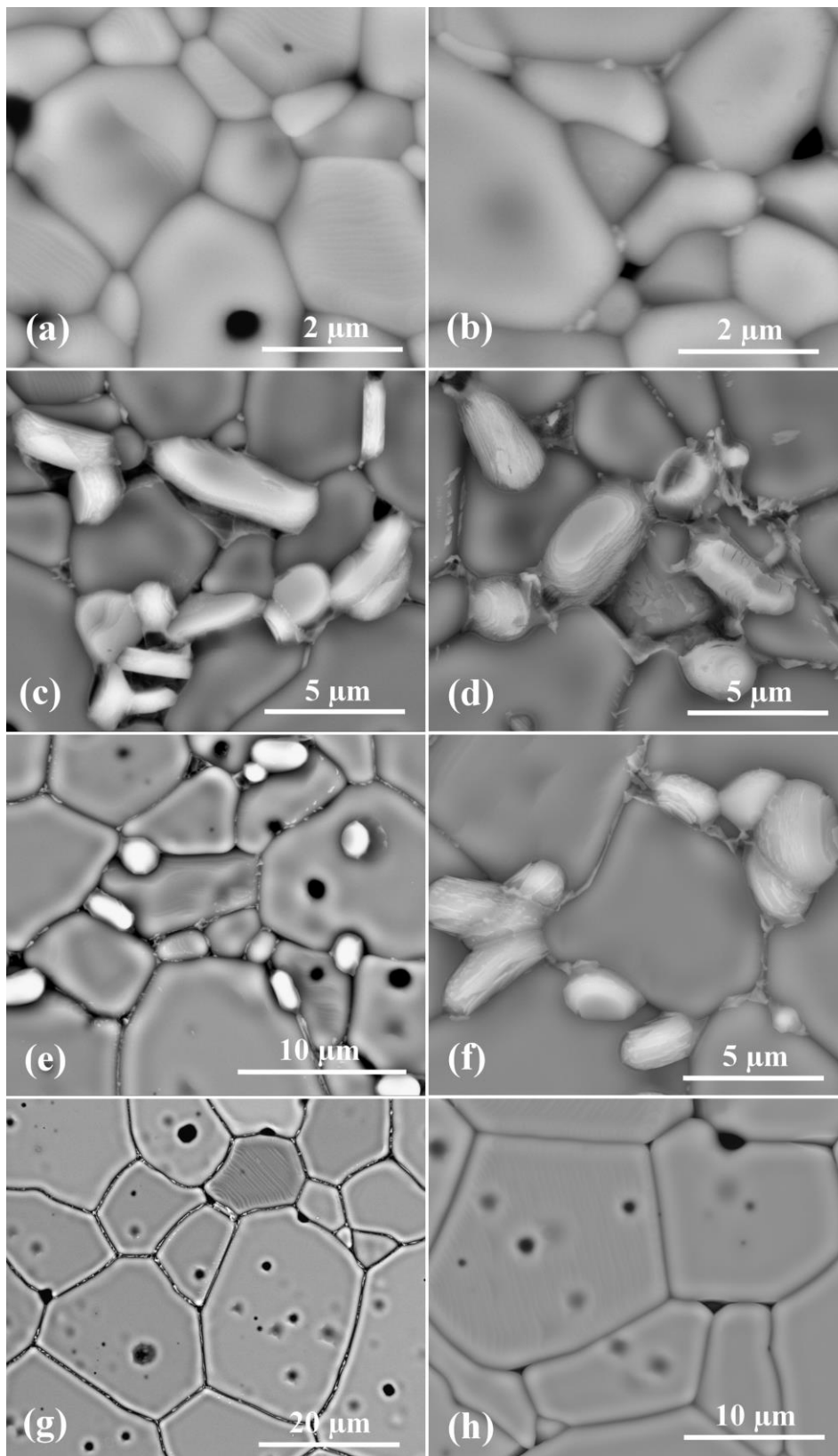


Fig. 2. Evolution of the microstructure of the samples against sintering time at a sintering temperature of 1100°C: (a) 0 h, (b) 0.2 h, (c) 0.5 h, (d) 1 h, (e) 2 h, (f) 5 h, (g) 15 h and (h) 30 h.

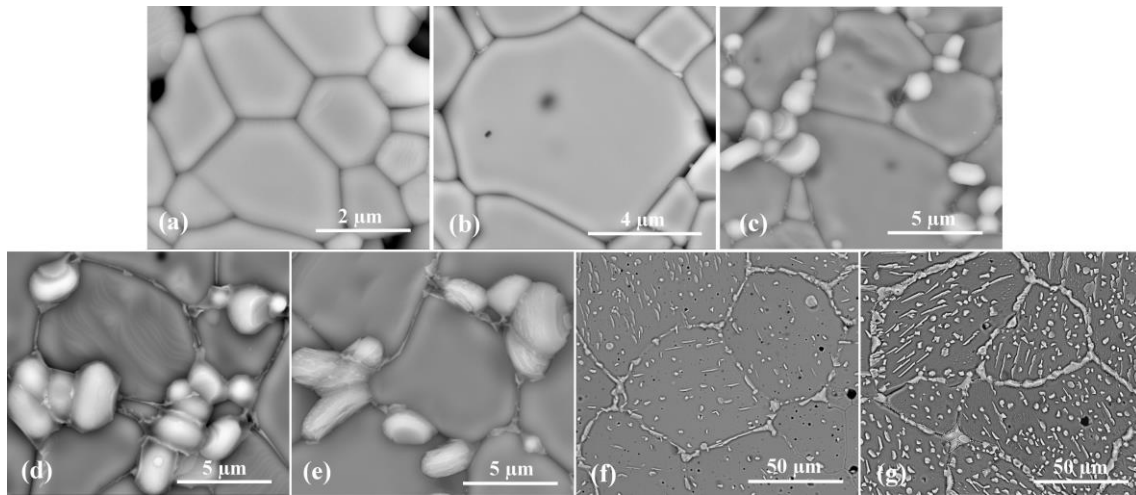


Fig. 3. Evolution of the microstructure of the samples against sintering temperature at a sintering time of 5 h: (a) 1000°C, (b) 1025°C, (c) 1050°C, (d) 1075°C, (e) 1100°C, (f) 1150°C and (g) 1200°C.

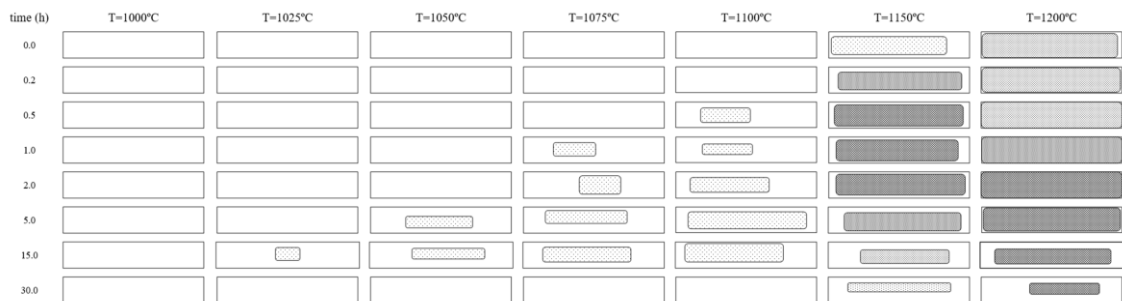


Fig. 4. Evolution of the cross-sectional area occupied by crystal precipitates and precipitated crystal density against sintering temperature and sintering time.

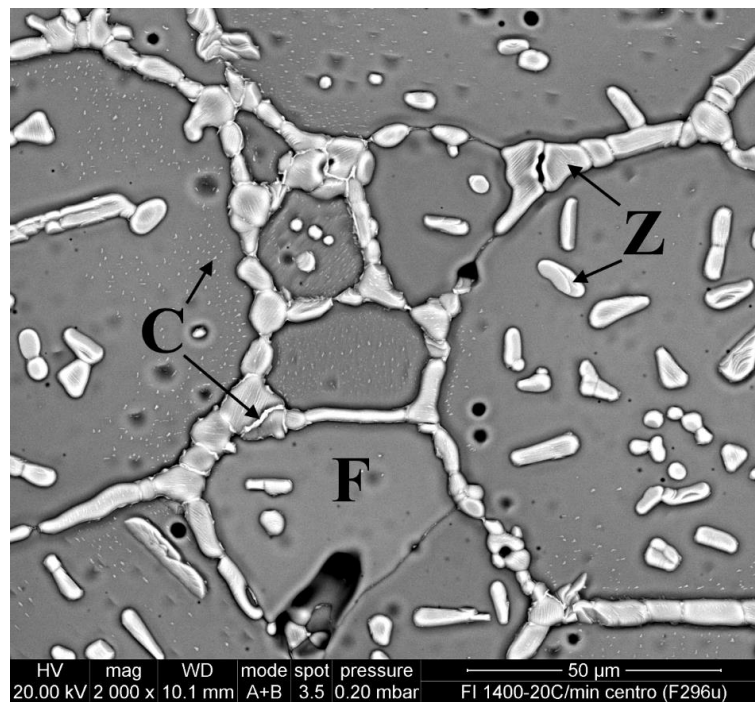


Fig. 5. Cross-sectional SEM micrograph showing the microstructure and grain boundaries of a sintered specimen with crystal precipitates.

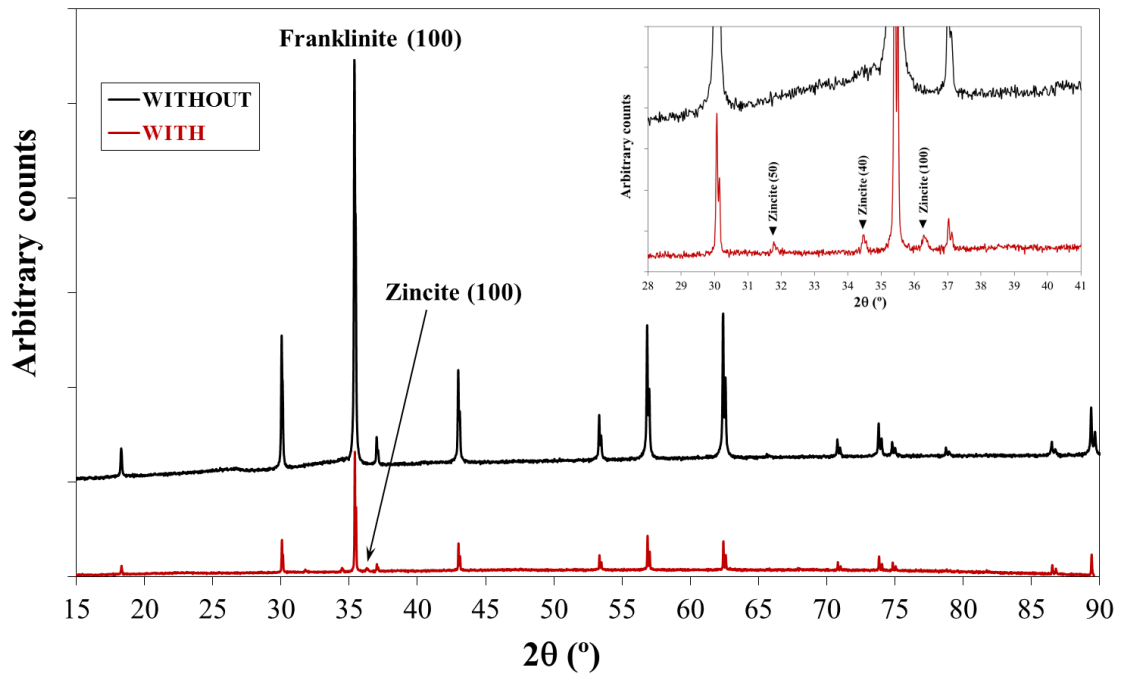


Fig. 6. XRD diffractograms of two sintered specimens, with and without crystal precipitates.

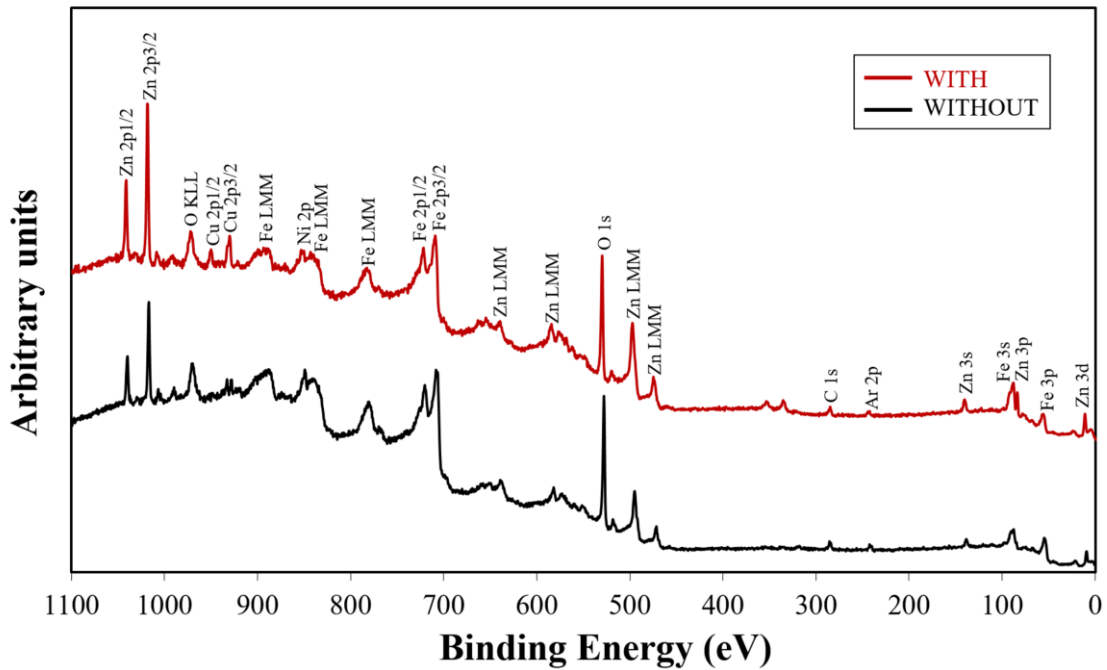


Fig. 7. Cross-sectional XPS spectra of two sintered specimens, with and without crystal precipitates.